Projection of upwelling-favorable winds in the Peruvian upwelling system under the RCP8.5 scenario using a high-resolution regional model

Adolfo Chamorro Gómez, Vincent Echevin, Cyril Dutheil, Jorge Tam, Dimitri Gutiérrez, François Colas

Projection of upwelling-favorable winds in the Peruvian upwelling system under the RCP8.5 scenario using a high-resolution regional model

Adolfo Chamorro (1,2), Vincent Echevin (2), Cyril Dutheil (2,3), Jorge Tam (1), Dimitri Gutiérrez (1,4), Francois Colas (2)

e-mail: achamorro@imarpe.gob.pe

(1) Instituto del Mar del Perú (IMARPE), Callao, Perú

(2) LOCEAN-IPSL, Sorbonne Université/IRD/CNRS/MNHN, Paris, France

(3) Department of Physical Oceanography and Instrumentation, Leibniz Institute for Baltic Sea Research Warnemünde, Rostock, Germany

(4) Laboratorio de Ciencias del Mar, Facultad de Ciencias y Filosofía, Universidad Peruana Cayetano Heredia, Lima, Perú

Abstract. The Peruvian upwelling system (PUS) is the most productive Eastern Boundary Upwelling System (EBUS) of the world ocean. Contrarily to higher latitude EBUSs, there is no consensus yet on the response of upwelling-favorable winds to regional climate change in this region. Global climate models are not able to reproduce the nearshore surface winds, and only a few downscaling studies have been performed by using relatively coarse-grid atmospheric models forced by idealized climate change scenarios. In the present study, the impact of climate change on the PUS upwelling-favorable winds was assessed using a high resolution regional atmospheric model to dynamically downscale the multi-model mean projection of an ensemble of thirty-one CMIP5 global models under the RCP8.5 worst-case climate scenario. We performed a 10-year retrospective simulation (1994-2003) forced by NCEP2 reanalysis data and a 10-year climate change simulation forced by a climate change forcing (i.e. differences between monthly-mean climatologies for 2080-2100 and 1989-2009) from CMIP5 ensemble added to NCEP2 data. We found that changes in the mean upwelling-favorable winds are weak (less than 0.2 m s-1). Seasonally, summer winds weakly decrease (by 0-5%) whereas winter winds weakly increase (by 0-10%), thus slightly reinforcing the seasonal cycle. A momentum balance shows that the wind changes are mainly driven by the alongshore pressure gradient, except in a local area north of the Paracas peninsula, downstream the main up-

welling center, where wind increase in winter is driven by the shoreward advection of offshore momentum. Sensitivity experiments show that the North-South sea surface temperature gradient plays an important role in the wind response along the north and central coasts, superimposed onto the South Pacific Anticyclone large-scale forcing. A reduction (increase) of the gradient induces a wind weakening (strengthening) up to 15% (25%) off the northern coast during summer. This local mechanism is not well represented in global climate models projections, which underlines the strong need for dynamical downscaling of coastal wind in order to study the impact of climate change on the Peruvian upwelling ecosystem.

Keywords

Regional climate change - Peruvian upwelling system - Upwelling-favorable wind - Ocean-atmosphere interactions

1. Introduction

The Peruvian Upwelling System (PUS) is located on the northern part of the Humboldt Current System, one of the four major Eastern Boundary Upwelling Systems (EBUSs) in the global ocean. It extends approximately between 4°S and 16° S along the western coast of South America and produces more fish catch per unit area than any other region (e.g. Chavez et al., 2008). There, as in other EBUSs, equatorward alongshore winds generate an offshore transport of coastal surface waters, which are replaced by subsurface colder and nutrient-rich waters. The cold surface waters influence the regional climate by creating a persistent low cloud cover (e.g. Mechoso et al., 2014) and the nutrient enrichment produced by the upwelling sustains a very high biological productivity (e.g. Cushing, 1990).

As other coastal upwelling systems, the PUS is expected to be impacted by the global warming associated to the continued increase of greenhouse gases in the atmosphere. Gutierrez et al. (2011) suggests that the coastal upwelling may have increased off Central and South Peru, driving a negative sea surface temperature (SST) trend between 1950 and 2010. The cooling is consistent with a wind increase found in the ERA40 reanalysis, suggesting a possible intensification of wind-driven upwelling. Unfortunately, instrumental records of multi-decadal nearshore wind variability are scarce in the PUS. Using in situ wind observations from the International Comprehensive Ocean Data Set (ICOADS; Worley et al., 2005), Bakun (1990) found an increase in nearshore wind stress in the period 1950-1990 in all EBUSs including the PUS, which led him to propose the ‘Bakun hypothesis’: the increase

of upwelling-favorable winds is driven by an increased cross-shore pressure gradient (due to low pressure over land and high pressure over sea), generated by an enhanced land-sea thermal contrast under climate change. However, Tokinaga and Xie (2011) showed that the alongshore wind positive trend in ICOADS observations was partly biased because of the increase in anemometer height of ship masts. Furthermore, Narayan et al. (2010) highlighted the large discrepancies between the PUS wind stress trends from ICOADS, NCEP/NCAR and ERA-40 reanalyses.

On the other hand, only a few studies based on global climate models have analyzed the response of upwelling-favorable winds to climate change in EBUSs, including the Humboldt Current System. Using the Coupled Model Intercomparison Phase 5 (CMIP5) ensemble, Rykaczewski et al. (2015) compared surface winds during the 2071-2100 period under the Representative Concentration Pathway (RCP) 8.5 to those during the 1861-1890 historical period. They found an intensification of upwelling-favorable winds in the poleward parts of EBUSs and a weakening in their equatorward parts. These changes were associated with a poleward migration of the high pressure systems (e.g. the South Pacific Anticyclone (SPA) for the Humboldt Current System). However, the PUS was not considered in their analysis as the latitudinal domain was limited to 16°S-44°S. Using the ensemble mean of thirty-one CMIP5 global climate models (see Table 1) for the 2080-2100 period relative to 1989-2009 period under the RCP8.5 scenario, the projected 10-meter wind changes are weaker (< 0.5 m/s) off the Peru coasts (3°S-18°S) than off Chile (18°S-40°S) (Fig.1a). Note that the coastal wind changes are not robust among the CMIP5 ensemble members, except south of 16°S and north of 6°S (red dots in Fig. 1a). Seasonally, alongshore winds tend to decrease in the north of Peru (5°S-9°S) in summer and tend to increase in winter south of 12°S (Fig. 1b). The relative changes are weak (< 5%), except near 5°S in summer (~30%). The marked differences between the wind changes off Peru and Chile suggest that the PUS winds could be influenced by other mechanisms than those related to the migration and intensification of the SPA (e.g. Rykaczewski et al., 2015).

Furthermore, only a few regional studies focused on the impact of the climate change on the PUS coastal winds using downscaling. Goubanova et al. (2010) used a statistical downscaling method to obtain surface wind at ~50 km resolution from the coarse-resolution (~300 km) CMIP3 IPSL-CM4 global model (Marti et al., 2010). They found that surface alongshore winds off Peru changed only during summer (5–10% weakening) under the idealized climate scenarios simulating a doubling (2xCO2) and a quadrupling of CO2 (4xCO2) concentrations with respect to preindustrial conditions. On the other hand, Belmadani et al. (2014) used a global atmospheric model with a progressively refined horizontal resolution of 0.5° × 0.5° in the Humboldt Current system, forced by IPSL-CM4 SST from the same scenarios as downscaled by Goubanova et al. (2010). They found that winds off Peru weakened

both during summer (20-30%) and winter (5-10%). The weaker winds were associated to the SPA southward shift and to the convective anomalies associated to the increased precipitation in the tropics during summer.

Nevertheless, the scope of these studies is limited in several ways: the wind projections remain relatively coarse-grid (~50–100 km), only one CGCM (IPSL-CM4) was downscaled under idealized scenarios (2xCO2 and 4xCO2). Moreover, mesoscale SST patterns can have an impact on the wind intensity (e.g. Chelton et al. 2001; Small et al. 2008). Chamorro et al. (2018) have recently shown that pronounced coastal SST alongshore gradients which appear under El Niño conditions reinforce coastal winds off Peru. This mechanism, which may play a role if latitudinal SST gradients are modified by climate change, has not been considered in previous studies.

In the present work, we expand on previous studies by assessing the coastal wind projections off Peru following a different approach. We use a high resolution regional atmospheric model forced by the multi-model mean (MMM) of thirty-one CMIP5 models under the worst-case Representative Concentration Pathway 8.5 (RCP8.5) scenario, for which the radiative forcing reaches 8.5 W m² by the year 2100 (van Vuuren et al. 2011). Using the regional model, we are able to study the mechanisms governing local wind changes and relate them to previous findings. Section 2 presents the CMIP5 ensemble, the regional settings, the data used to evaluate the model's realism and the methods. Section 3 presents the model results: an evaluation of surface winds in the present period, the projected wind and SPA changes, and a surface momentum budget. A summary and discussion of the main results are presented in section 4.

2. Model, data and methods

2.1 The regional atmospheric model

We used the Weather Research and Forecasting (WRF, Skamarock and Klemp, 2008) model version 3.7.1 with three nested domains (Fig. 2a). The largest domain (d01) encompasses the tropical-subtropical South Pacific ocean (42°S-26°N; 101°E-58°W) with a horizontal resolution of 105 km and 210 x 78 grid points. This so-called parent domain has a wide extension as it was also used to carry out climate change projections in the South Pacific Convergence Zone (Dutheil et al., 2019). The second domain (d02) covers the coasts of Peru and Northern Chile (30°S-10°N; 101°W-63°W) with a horizontal resolution of 21 km and 200 x 220 grid points. The innermost domain (d03) covers nearly all of the Peruvian coastal segment (17°S-5°S) with a horizontal grid spacing of 7 km and

225 x 216 grid points. The high resolution of the latter allows to better represent the Andes and the coastal orography (Fig. 2b). 32 levels in the vertical were used in the parent domain, while 60 levels in the vertical were used in the second and innermost domain, with 21 levels in the first ~1000 m above sea surface, following Oerder et al (2016). The model time steps were set to 300, 45 and 15 s for the domains of 105, 21 and 7 km resolution, respectively. The three different configurations are hereafter referred to as WRF105, WRF21 and WRF7.

The set of physical parameterizations used in the model are similar to those used in Chamorro et al. (2018). They include the Dudhia (1989) and Mlawer et al. (1997) schemes for shortwave and longwave radiation respectively, the Hong and Lim (2006) microphysics scheme, the Betts-Miller-Janjić parameterization for convection (Janjić 1994), the Mellor–Yamada– Nakanishi–Niino (MYNN) Level 2.5 planetary boundary layer (Nakanishi and Niino 2009) along with the MYNN surface layer parameterization, and the Noah land surface model (Chen and Dudhia 2001).

2.2 Historical and climate change experiments

First, a control simulation was carried out for the retrospective period 1994-2003 in the three nested domains in one-way offline nesting mode (i.e. a finer-grid-resolution run is made as a subsequent run after the coarser-grid-resolution run). The initial and lateral boundary conditions for the finer-grid run are obtained from the coarse grid run. Input from terrestrial fields (e.g. terrain, land use, etc.) and masked surface fields (such as soil temperature and moisture) are obtained from WRF geographical datasets (available in http://www2.mmm.ucar.edu/wrf/users/download/get_sources_wps_geog.html). The parent domain is forced by lateral open boundary conditions from the 6-hourly NCEP2 reanalysis data at 1° (Kanamitsu et al., 2002) and by daily Optimum Interpolation Sea Surface Temperature (OISST) data at 0.25° (Reynolds et al. 2007) at the air-sea interface. In this simulation, the atmospheric CO_2 concentration is increased from 358 to 375 ppm (levels representative of the retrospective period).

Second, a climate change simulation was performed for a ten-year period (2086-2095) in the three nested domains in one-way offline nesting mode, following the pseudo global warming downscaling method (PGW-DS, Kimura and Kitoh, 2007). The ensemble mean from thirty-one CMIP5 global models (see Table 1) of monthly anomalies of the seasonal cycle were added to the 6-hour NCEP2 lateral atmospheric boundary conditions, following the same methodology as in Dutheil et al. (2019). The monthly anomalies of the ensemble-mean seasonal cycle are differences between the monthly ensemble-mean seasonal cycle computed over the period 2080-2100 under the RCP8.5 scenario and the monthly ensemble-mean seasonal cycle computed over the historical period 1989-2009. The ensemble-mean RCP8.5 historical annual-mean SST anomaly displays a strong surface warming of 3-4°C

along the Peru coasts (Fig 3a). The monthly anomalies were added to the NCEP2 6-hourly air temperature, water vapor mixing ratio, geopotential height, zonal and meridional wind at each vertical level of the model, and also to the daily OISST sea surface temperature (Reynolds et al., 2007). The land parameters were kept identical to the control simulation. In this simulation, the atmospheric CO_2 concentration is increased from 810 to 890 ppm. These levels are representative of the RCP8.5 projections at the end of the twenty-first century for the period 2086-2095 (Van Vuuren et al., 2011).

The PGW-DS method adds a climate perturbation signal to a present-day conditions in order to obtain future climate conditions at a higher resolution. This approach also allows to remove the present-day biases of CMIP5 models and cancels the variable part of errors from individual models when multi-model mean anomalies are used (Kawase et al. 2008). Using the ensemble mean of a large ensemble of coupled model simulations (e.g. 30) reduces the uncertainty caused by the low-frequency variability and highlights the impact of external greenhouse gas forcing (Jebri et al., 2020), even in the case of a relatively short integration period (e.g. ten years), regardless of the selected control period (Kawase et al., 2009). However, this approach has some limitations that should be kept in mind when interpreting the results. The intra-seasonal and interannual variabilities in the lateral and surface boundaries conditions for the 2086-2095 period are identical to those of the 1994-2003 period. In other words, the anomaly related to the strong 1997-1998 El Niño is encountered in 2083-2084 under the RCP8.5 scenario. Thus, the possible change of El Niño variability under the RCP8.5 scenario and its local impact in the PUS are not simulated in this study.

In addition, three sensitivity experiments were performed using WRF21 for ten-year periods under RCP8.5 scenario. They were forced by the same multi-model mean lateral atmospheric boundary conditions as previously described, and by SST anomalies from CESM1-CAM5, CNRM-CM5 and CSIRO-Mk3-6-0 climate models instead of the multi-model mean. These simulations were used to assess the sensitivity of the coastal wind projections to the along-shore SST gradient. These particular climate models simulated distinct alongshore SST gradient changes in RCP8.5 conditions with respect to the historical period: around zero, negative and positive (see CGCM numbers 8, 11 and 12 respectively in Fig. 3b). The three downscaled simulations are called WRF-cesm1, WRF-cnrm and WRF-csiro.

2.3 Monthly momentum budget

Changes in the momentum budget was analyzed following the method described in Oerder et al. (2016) and Chamorro et al. (2018). We used the following vectorial relation:

$$\langle V\rangle_{M+1} - \langle V\rangle_{M} = \sum_{F_n \in [\text{forces}]} \Delta t \left([F_n]_{M+1} - [F_n]_{M} + \langle F_n \rangle \right) \quad (1)$$

where, $\langle V \rangle$ is the wind monthly-mean vector, Δt is the model time step, and F_n are the four momentum terms: advection $\left(\vec{v}.\vec{\nabla}\right)\vec{v}$, vertical mixing $\frac{\partial}{\partial z}\left(\frac{\vec{\tau}}{\rho}\right)$, Coriolis $-f\,\vec{k}\,x\,\vec{v}$ and pressure gradient $\frac{-1}{\rho}\vec{\nabla}P$, such as the left side of Eq. (1) represents the change of the wind monthly-mean V (from month M to month M+1) and the right side of the equation represents the sum of the forces contributions (F) to the momentum balance. The angle bracket ([ ]) in Eq. (1) is the double time averaging operator defined as:

$$[F_n] = \frac{1}{N+1} \sum_{p=0}^{N} \left(\sum_{k=1}^{p} F_n \right) \quad (2)$$

with N the number of model time steps during one month. We computed the alongshore (i.e. parallel to the WRF model smoothed coastline) component of Eq. (1) in four coastal boxes (between 5-8°S, 8-13°S, 13-14°S and 14-17°S) of one-degree width along the coast of Peru.

2.4 Observational data

Surface wind observations from the QuikSCAT satellite-borne scatterometer (CERSAT, 2002; hereafter QSCAT) at 1/2° resolution were used to evaluate the realism of the modeled wind over the period 2000-2003. The product was downloaded from http://www.ifremer.fr/cersat.

The Pearson correlation coefficient (r) was used to measure the strength of a linear association between two variables, and a p-value less than 0.01 was used to determine the statistical significance of the relationship.

3. Results

3.1 Evaluation of the mean and seasonal cycle of present-day coastal winds

In order to evaluate the impact of the model resolution on surface winds, the 2000-2003 annual mean surface wind from WRF105, WRF21 and WRF7 are shown in domain d03 in Figs. 4a-c. Observations (Fig. 4d) indicate that surface winds blow north-westward in a direction approximately parallel to the coastline. The wind is strongest offshore (~6-7.5 m s-1) and decreases shoreward down to ~4.5-5 m s-1. Offshore winds are slightly overestimated

(~1 m s-1) in the model simulations, regardless of the spatial resolution. The wind intensification off the Paracas peninsula (14°S) is too strong in WRF21 (Fig. 4b) but likely more realistic in WRF7 (Fig. 4c). The near-shore wind decrease from ~200 km towards the coast (a.k.a. 'wind drop-off', *e.g.* Capet et al., 2004) off the central coast (7°S-12°S) is relatively well reproduced in WRF7, whereas it is overestimated in WRF105 and underestimated in WRF21 (Fig. 4e). Note that the wind drop-off in the 0–50 km coastal band is not well known due to the so-called 'satellite blind zone'.

Figure 5 shows the WRF7 and QuikSCAT mean annual cycle of alongshore wind averaged in a coastal band of ~100 km, for the period 2000-2003 (when satellite observations are available). Observed winds are weakest in summer, reaching a minimum of ~ 3-4 m s^{-1} off the center and north coast (5°S-12°S), and strongest in winter, reaching a maximum of ~ 7 m s^{-1} near 15°S (Fig. 5a). Overall, WRF7 reproduces well the seasonal cycle of along-shore winds in good agreement with satellite observations, replicating the local maximun value near 15°S in win-ter. However, some discrepancies are found, such as an overestimation (~ 1 m s^{-1}) of the alongshore wind intensity off central Peru (8°S-15°S) in summer and a slight underestimation (<1 m s^{-1}) in winter-spring (Fig. 5c). Note that QuikSCAT data does not include information of wind in the satellite blind zone, which may explain some of the discrepancies.

Overall, these comparisons show that WRF7 reproduces the mean state and seasonal variability of coastal winds off Peru with a fair degree of realism. The surface wind bias in the coastal region due to coarse horizontal resolu-tion has been an important limitation of previous modeling studies (e.g. Belmadani et al., 2014; Oerder et al., 2015).

3.2 Climate-driven changes in coastal wind

The projected wind changes simulated are now characterized by the different model configurations. We focus on WRF21 and WRF7 wind changes, because of WRF105 too coarse spatial resolution. WRF21 and WRF7 show weak (and very similar) changes in the mean surface wind field (Figs. 6 a-b, d-e). Wind velocity increases slightly in the offshore region (400 km from the coast) by about 0.2 m s-1. In the nearshore region, wind velocity decreases slightly (<0.2 m s-1) off the north and south coast of Peru, and increases slightly off the central coast (9°S-13°S). The increase in the nearshore region (11–14°S) is larger in WRF7 (~0.2 m s-1) than in WRF21 (~0.1 m s-1). Ex-amination of the alongshore wind seasonal cycle (Figs. 6 c, f) reveals more pronounced differences among the coastal regions. The winds tend to weaken in spring and summer (by ~5 %) off the north (5°S-9°S) and south

(14°S-17°S) coasts, and alongshore winds tend to intensify in fall and winter off the central coast by ∼5 % in WRF21 and ∼10 % in WRF7. Overall, the relative changes do not exceed 5-10% which contrasts with the stronger change (e.g. up to a 30 % reduction in summer near 5°S) in the CMIP5 ensemble mean (Fig. 1b). Besides, the resolution increase from 21 km to 7 km did not strongly modify the results, except the slightly stronger winter wind intensification off central Peru (9°S-14°S).

3.3 Changes in the structure of the SPA

As suggested by previous studies (e.g. Rykaczewski et al., 2015; Belmadani et al., 2014), changes in the SPA are expected to impact the nearshore winds in the PUS. In this section the characteristics of the SPA are investigated in the WRF105 simulation (which provides lateral boundary conditions to WRF21). The SPA reaches its southernmost position and is weakest in summer (Fig. 7a). It is shifted southwestward and sea level pressure (SLP) at its center increases by ∼2 hPa under RCP8.5 scenario with respect to the retrospective period (1994-2003). This coincides with a slight SLP decrease (∼-1 hPa) along the Peru coasts. In contrast, the SPA is located at its northernmost position and is more intense during winter (Fig. 7b). Its position does not change much under RCP8.5 (black lines in Fig. 7b) but SLP increases by ∼2 hPa at its center. These changes may impact the alongshore pressure gradient off Peru, a potential driver of alongshore wind changes.

3.4 Climate-driven changes in the momentum budget

In order to investigate the dynamical processes associated with the wind change off Peru, a monthly alongshore momentum budget (see section 2.3) is performed in four coastal boxes of ~100 km width between 5-8° S, 8-13°S, 13-14°S and 14-17°S using WRF7 outputs (see boxes in Fig. 8a) for summer (Fig.8) and winter (Fig.9). The main equatorward force in the alongshore wind direction (i.e. equatorward) is the alongshore pressure gradient, (light blue bars in Fig. 8b,9b), that is mainly balanced by the vertical mixing term (i.e. friction over the sea surface, yellow bars in Fig. 8b,9b) during both seasons. This balance takes place along most of the coasts except between 13-14°S (off Pisco bay). There, the equatorward pressure gradient is much weaker: advection of momentum drives the coastal wind and is balanced by friction. Note that the alongshore component of the Coriolis force is weaker than the other terms as the wind direction is mainly alongshore.

In RCP8.5 summer conditions, the pressure gradient decreases all along the coast (light blue bars in Fig. 8c). The decrease is stronger between 14–17°S than in other coastal sectors. The alongshore pressure gradient decrease is

consistent with the SPA poleward shift during summer (Fig.7a). The pressure gradient weakens more between 5°S-8°S than between 8°S-13°S, suggesting that at low latitudes (5°S-8°S) another process may take place over the effect of the SPA poleward displacement (see section 3.6). The pressure gradient decrease is mainly equilibrated by a change in Coriolis force near 13°S-17°S, due to the change of wind direction toward the land (Fig.8a). This direction change could be attributed to the meridional shift of the SPA (Fig.7a).

In RCP8.5 winter conditions, the pressure gradient tends to increase between 13°S–17 °S and less between 8-13 °S, in contrast with summer conditions (Fig.9c). This is in line with the large scale SLP intensification during this season (Fig.7b). Advection of momentum also tends to increase near Pisco Bay (13°S-14°S) but also along a large coastal sector (8°S-13°S), playing a stronger role than the pressure gradient on the wind acceleration.

3.5 Local wind intensification to the north of Paracas peninsula (13°S-14°S)

The coastal area north of the Paracas Peninsula and Pisco area (13°-14°S) is located downstream the main upwelling area off Peru and stands out as a segment where the momentum balance is different from other coastal areas (Figs. 8b, 9b). Furthermore it is the region of maximum wind winter intensification under RCP8.5 conditions (Figs. 6c, f). For these reasons, the momentum budget deserves a particular examination here (it is also interesting to mention that this area sustains very important tourism and aquaculture activities; e.g. Aguirre-Velarde et al., 2019). In order to investigate in more details the respective contributions (zonal, meridional and vertical advection) to the total meridional momentum advection term driving the wind change in this area, we computed these terms offline from the velocities in present and RCP8.5 future conditions, using the following:

$$V_{ADV} = -U\frac{\partial V}{\partial x} - V\frac{\partial V}{\partial y} - W\frac{\partial V}{\partial z} \quad (3)$$

where V_{ADV} is the total advection of meridional momentum, $-U\frac{\partial V}{\partial x}$ is the zonal advection term, $-V\frac{\partial V}{\partial y}$ is the meridional advection term, and $-W\frac{\partial V}{\partial z}$ is the vertical advection term (of the meridional momentum).

We found that downwind of the Paracas peninsula, the advection term accelerates the meridional wind in late fall-early austral winter (May-August) present conditions (Fig. 10a). Similar results have been reported in modelling studies of expansion fans near capes (e.g. Perlin et al., 2011; Soares et al. 2018). The meridional wind acceleration

is mainly due to meridional advection (Fig. 10b), while zonal advection is weak, excepted in the inner bay where the intensities are comparable (not shown). The contribution of the vertical advection term is negligible everywhere (not shown). Expectedly, the large-scale pressure gradient forced by the SPA is unable to generate a strong pressure gradient in and slightly north of the Paracas bay (Figs. 8b, 9b) as this area is shielded by topographic obstacles blocking the pressure force, as illustrated by a much weaker wind change in WRF21 (0.5 vs 1.0 m s-1; Fig. 6cf).

Under RCP8.5 conditions, the acceleration increase due to the advection term increase (Fig. 10c) is mainly related to the change in meridional advection ($-V.\partial V/\partial y$; Fig. 10d), in line with the increase in alongshore velocity offshore of the bay (Fig. 9a). Small-scale positive changes in zonal and vertical advection occur only nearshore just north of Paracas bay and around the peninsula, respectively (not shown).

3.6 Sensitivity of coastal wind change to alongshore SST gradient change

In the following, the sensitivity of wind change to alongshore SST gradient changes is investigated as in Chamorro et al. (2018) under El Niño conditions. These authors showed that an equatorward alongshore temperature gradient, such as the one encountered in the presence of anomalously warm waters in the north of Peru, may generate a pressure gradient and an equatorward wind anomaly. As shown in Figure 3b, the slight decrease of the alongshore SST gradient (~-0.2 °C per 1000 km, i.e. the SST increase is slightly weaker in the north than in the south of Peru) may contribute to weaken the alongshore pressure gradient and thus the wind intensity during summer (Fig. 8), particularly in the north of Peru, and possibly to compensate part of the wind increase during winter (Fig. 9).

Figure 11 shows Hovmöller latitude-time diagrams of the absolute (colours) and relative (contours) change in alongshore wind for the three WRF sensitivity experiments described in section 2.2. The simulation WRF-cnrm was forced by a stronger negative alongshore SST gradient change than the ensemble mean (~-0.5°C per 1000 km, see bar n°11 in Fig.3b). It shows a weakening of the alongshore wind in the north coast with a relative wind change of -15% and -10% in summer and spring respectively (Fig. 11a). The winter wind increase in central Peru (9°S-13°S) is also weaker than in the ensemble-mean simulation (Fig.6c). In contrast, the simulation WRF-csiro was forced by a positive alongshore SST gradient change (~0.6°C per 1000 km, see bar n°12 in Fig.3b), of opposite sign than the ensemble mean. This results in a sustained intensification of the alongshore winds in the north of Peru (5°S-10°S) with maxima in relative wind change of +30% and +20% in summer and spring respectively (Fig. 11b). The third simulation, WRF-cesm1, forced by a very weak (~0.05 °C per 1000 km, see bar n°8 in Fig.3b)

coastal alongshore SST gradient change, shows alongshore wind relative changes less than 10% (Fig. 11c). The patterns are quite similar to those of the control simulation (Fig.6c), however the wind slackening in summer is weaker than that of the control simulation, and the wind increase in winter is stronger than that of the control simulation. Note that the alongshore wind changes in the southern sector (14°S-18°S) do not vary as much in the three sensitivity experiments and in the control simulation, which suggests that the wind changes off southern Peru are less forced by SST changes, and likely rely more on large scale changes associated with the SPA (which are similar in the four simulations).

These results confirm that alongshore wind projections in the north and central coast off Peru are sensitive to changes in alongshore SST gradient, as during El Niño events (Chamorro et al., 2018). The seasonal response of the alongshore winds to the local alongshore SST gradients is further investigated in detail in the northern, central and southern coastal sectors. In most cases, SST gradient changes are weaker than 1°C per 1000 km in the northern sector, but strong SST and wind changes may occur during summer (Fig.12a). SST gradient and wind change occur all year long in the central sector (Fig.12b). The wind response to local SST change is stronger in summer-spring (r=0.84-0.87) than in fall-winter (r=0.53-0.7). Indeed, as the SPA is located further south in summer (Fig. 7a), the local pressure gradient driven by the alongshore SST gradient may play a more important role than the large-scale one associated with the SPA. As shown in Fig.11, the relation between changes in alongshore SST gradient and coastal wind is non-existent in the south sector (r= 0.01, Fig. 12c).

4. Discussion and conclusions

4.1 Summary

Regional dynamical downscaling using a high resolution regional atmospheric model was performed to study the impact of climate change on upwelling-favorable surface winds in the PUS. The WRF regional model was applied using three nested domains with 105, 21 and 7 km of horizontal resolution. We performed a control simulation forced by the NCEP2 reanalysis for the period 1994-2003, and a climate change simulation where the ensemble-mean monthly anomalies from thirty-one CMIP5 global models forced under RCP8.5 were added to the NCEP2 lateral boundary conditions and SST. The high- resolution atmospheric simulation (WRF7) reproduced well the intensity and seasonal variability of alongshore winds, as well as the mean wind drop-off near the coast. The downscaling of the RCP8.5 ensemble resulted in weak changes in the annual-mean alongshore winds off Peru with respect to the control simulation. In general, winds tended to decrease weakly in spring-summer (~0-5%) and to increase weakly in fall-winter (~5-10 %), which corresponds to a slight intensification of the seasonal cycle. The

WRF7 simulation was able to represent a local relatively strong intensification of the nearshore winds between ~10-14°S during winter thanks to its fine grid.

A momentum balance shows that over most of the coastal region the alongshore pressure gradient is the dominant force driving the surface wind acceleration. Under the climate change scenario, the pressure gradient decreases in summer and increases in winter, driving the weakening and/or intensification of the winds off the coast respectively. As the nearshore region between ~13-14°S located north of the Paracas-Pisco bay area is protected by coastal topography, horizontal advection of momentum plays a crucial role on the wind dynamics. In particular, the enhanced offshore momentum during winter is advected to the Pisco bay area, resulting in a strong local wind intensification (~10 %). Note that the wind remains nevertheless weaker downwind than upwind of the cape.

RCP8.5 changes in alongshore winds seem to be driven for a good part by changes in the large-scale atmospheric circulation, which may impact the alongshore pressure gradients off Peru. The decrease of the RCP8.5 PUS coastal winds during summer could be associated to the SPA south-westward displacement, even though the SPA becomes slightly more intense (+2 hPa, Fig. 7a). In contrast, the coastal winds intensification during winter is consistent with the strong SPA intensification (+4 hPa, Fig. 7b). These results suggest that the projected coastal winds off Peru are sensitive to the changes in the position and intensity of the SPA, in agreement with previous studies (Belmadani et al., 2014).

Sensitivity simulations using different SST conditions than the ensemble-mean indicate that the alongshore SST gradient acts as a local forcing superimposed onto the SPA large-scale forcing. It is able to modulate significantly coastal winds off central-north Peru (e.g. like the intensification of coastal winds due to an increased north-south SST difference during El Niño studied by Chamorro et al., 2018). Long-term changes in the alongshore SST gradient off Peru are likely related to the evolution of El Niño under climate change: we could speculate that in case of more frequent or more intense Eastern Pacific El Niño events (Cai et al., 2014), a stronger SST gradient and more intense coastal winds may be expected, whereas more frequent Central Pacific events may trigger the opposite situation (Yeh et al., 2009). In addition, the alongshore SST gradient off Peru could also have played a role in the recent SST trends described by Gutierrez et al (2011), since the cooling off the Central-South coast and the warming off the North coast (i.e. strengthening of the alongshore SST gradient) could have forced a coastal wind intensification, which in turn would force a coastal cooling. So, this may imply a negative feedback on the SST warming off

388 the coast (Echevin et al., 2020) and a positive feedback on coastal upwelling under climate change. However the
389 strength of these feedbacks remain to be investigated.

390

391 **4.2 Roles of the land-sea thermal contrast and low-latitude precipitation**

392 Bakun (1990) and Bakun et al. (2010) proposed that the land-sea thermal contrast may increase under climate-
393 change and induce alongshore wind increase. This would result from a stronger heating of the land mass, driving a
394 low pressure over land and enhancing the land-sea pressure gradient and the related along-shore geostrophic wind.
395 Wang et al. (2015) found a marked correlation between alongshore wind increase and land-sea thermal contrast at
396 higher latitudes in different EBUS (note that most of the Peru upwelling system was not included in the studied lat-
397 itude range) suggesting a link between nearshore winds and thermal contrast in those areas. Using a 50 km resolu-
398 tion model in the Peru region, Belmadani et al. (2014) found an increase in land-sea thermal contrast all along the
399 Peru-Chile coasts and a reduction of the alongshore pressure gradient and coastal winds off Peru. Our 7-km model
400 (WRF7) simulated an increase of the land-sea thermal gradient by ~20-25% (i.e. the same order of magnitude,
401 shown in Fig.8c from Belmadani et al., 2014) during summer and by 30-50% during winter (Figure not shown).
402 Thus, while we can not rule out a potential role of the land-sea thermal contrast in winter, it is clearly not the domi-
403 nant process during summer as winds decrease along most of the coastal range (Fig. 6).

404

405 Besides, Belmadani et al. (2014) suggested that part of the summer wind decrease in the north of Peru may be
406 caused by an increase of precipitation associated with convection, which produces surface wind convergence and
407 equatorward wind reduction. Our simulations also show an increase in precipitation in summer (not shown), but it
408 occurred more than 200 km away from the Peru coast, so that its contribution to the coastal winds decrease in sum-
409 mer may not be as strong as in Belmadani et al. (2014) simulations. Note that this precipitation effect depends on
410 the amplitude of the RCP8.5 SST anomalies in the north of Peru, and are not directly linked to the alongshore SST
411 gradient.

412

413 **4.3 Role of large-scale versus local processes on CMIP5 coastal wind projections**

414 We showed that changes in the ensemble-mean large-scale conditions (SLP) and local conditions (SST alongshore
415 gradient) strongly impact on the coastal winds in our downscaling approach. Here we investigate whether the dy-
416 namical relation between coastal wind change and SST gradient change may also be valid for the individual mem-
417 bers of the CMIP5 ensemble. In addition, we analyze the contribution of the large scale SLP change to the wind

changes. To this aim, we computed the large-scale sea level pressure (SLP) meridional gradient change between the tropical and subtropical regions and the alongshore SST gradient change off the Peru coast (computed as the difference of the SST averaged between 5-9°S and 9-13°S in a 200-km coastal band) for the 31 CMIP5 global models (Fig. 3b). The large-scale SLP meridional gradient was computed as the difference between the SLP maximum value in the subtropical eastern Pacific (i.e. the highest pressure in the center of the SPA) and the SLP minimum value in the tropical Pacific (between 0 and 20°S) at the same longitude of the center of the SPA (Fig 13a). We found that the coastal wind change off Peru coast from CMIP5 global models correlates significantly ($r=0.57$, $p<0.01$) with intermodels large-scale SLP meridional gradient change. The correlation is stronger in winter ($r=0.68$) and not significant in summer (Fig 13b). This is consistent with Rykaczewski et al. (2015) who found similar results for the southern Humboldt system (16°S-40°S). On the other hand, CMIP5 wind change and SST gradient change correlations are not significant ($p>0.01$; Fig. 13c). Global models are thus not able to reproduce the nearshore wind variability driven by the alongshore SST gradient change, likely due to a poor representation of the nearshore wind structure at coarse-resolution. This makes a strong argument in favor of the dynamical downscaling approach that was used.

4.4 Limitations and future work

A first limitation of our methodology lies in the construction of the SST field forcing WRF. Anomalies of the SST seasonal cycle from each CMIP5 model were interpolated from their ocean model grid onto a common 1°x1° grid, regardless of the resolution and coastline of the CGCM ocean model. It must be noted that differences between CGCM coastline shapes and positions can be quite important. The common 1°x1° SST anomalies were then linearly extrapolated in the nearshore region to force our high-resolution atmospheric climate change simulations. The two methodological steps could introduce unrealistic SST patterns that can impact on the coastal wind. This predicament can be solved by using a regional ocean-atmosphere coupled model with the same resolution in the ocean and atmosphere (e.g. as in Oerder et al., 2016, 2018) in which the ocean dynamics could correctly represent the nearshore SST field. Such an approach would also allow ocean-atmosphere feedbacks, which could modify the nearshore surface temperature and winds.

A second obvious limitation is the use of a single set of boundary conditions for RCP8.5 (the ensemble-mean in the present case). In the presence of a large variety of large-scale SLP gradients (Fig.13b), it would be interesting to select a limited number of models and investigate the impact of different large-scale conditions (e.g. different

SLP evolutions) from different large grid-scale climate models. This would be needed to improve the consensus on the wind projections in the Peruvian upwelling system for the end of the 21st century.

4.5 Conclusions

Using a dynamical downscaling method, we found that the climate-driven large-scale changes associated with the SPA impact coastal wind changes in the Peruvian Upwelling System but that these changes can be modulated by coastal topography and by alongshore sea surface temperature gradients. We have also shown that dynamical downscaling at scales of the order of 10 km is mandatory to tackle such subtle effects. In addition, this study has examined in details the impact of the RCP8.5 scenario in the PUS, the northern part of the Humboldt Current System that has been largely ignored in recent studies about future wind changes in EBUSs (e.g. Sydeman et al., 2014; Rykaczewski et al., 2015; Wang et al., 2015; Oyarzun and Brierley (2019) have systematically ignored the coastal sector north of 16°S). Overall, our results are partly in line with previous studies based on different and more extreme climate scenarios: we confirm the moderate weakening of coastal winds off Peru in summer, found in previous studies (Goubanova et al. 2011; Belmadani et al. 2014). However, we found a wind increase during winter off central Peru, constrasting with previous findings.

Such weakening of the alongshore wind in summer (and strengthening in winter) results in an enhanced seasonal cycle of the coastal winds off central Peru. This may impact on the productivity of the Peruvian upwelling system. Indeed the intensity of the wind controls the upwelling of nutrient-replete waters and the intensity of surface productivity (Echevin et al. 2008). Thus regional climate change may induce a less productive summer season because of an enhanced nutrient limitation and a less productive winter season because of an enhanced light limitation due to a thicker mixed layer (Echevin et al., 2008). Thus, a straightforward perspective of the present work is to study the impact of the downscaled RCP8.5 wind changes on the Peruvian ecosystem by forcing a regional biophysical model following the approach of Echevin et al. (2020). Furthermore, the wind weakening off Northern Peru in summer could generate more frequently coastal warming conditions, known as ‘Coastal El Niño’ (Takahashi and Martínez 2017; Garreaud 2018; Echevin et al., 2018) in the future, which should be investigated using a regional ocean-atmosphere coupled model. These issues will be the subject of future works.

5. Acknowledgments

This research is a product of the scientific cooperation between the Peruvian Marine Research Institute (IMARPE) and the Institut de Recherche pour le Developpement (IRD - France) in the framework of the IRD LMI DISCOH program. Numerical simulations were performed on TGCC Curie and Irene SKL High Performance Computers under projects A0050101140 and A0060101140. Nicolas Jourdain is acknowledged for processing the ensemble-mean lateral boundary conditions for the regional atmospheric model simulations. Francis Codron, Jose Rutllant, Pierrick Penven, Claude Estournel and Sebastien Masson are acknowledged for fruitful discussions.

J. Tam, D. Gutierrez and A. Chamorro acknowledge finantial support from the Adaptation Fund project "Adaptation to the Impacts of Climate Change on Peru's Coastal Marine Ecosystem and Fisheries". J. Tam, F. Colas and A. Chamorro acknowledge financial support from the project Concytec - World Bank, through Fund for Scientific, Technological, and Technological Innovation Development (Fondecyt), for the project "Characterization and forecast of extreme events in the Peruvian ocean using an operational system of oceanic information".

6. References

Aguirre-Velarde A, Thouzeau G, Jean ., Mendo J, Cueto-Vega R, Kawazo-Delgado M, Flye-Sainte-Marie J. (2019). Chronic and severe hypoxic conditions in Paracas Bay, Pisco, Peru: Consequences on scallop growth, reproduction, and survival. Aquaculture, 512, 734259.

Bakun, A., 1990. Global climate change and intensification of coastal ocean upwelling. Science 247 (4939), 198–201.

Bakun A, Field D, Renondo-Rodriguez A, Weeks SJ (2010) Greenhouse gas, upwelling favourable winds, and the future of upwelling systems. Glob Chang Biol 16:1213-1228

Belmadani A, Echevin V, Codron F, Takahashi K, Junquas C (2014) What dynamics drive future wind scenarios for coastal upwelling off Peru and Chile? Clim Dyn 43: 1893-1914. doi:10.1007/s00382-013-2015-2

Cai W, Borlace S, Lengaigne M et al. (2014) Increasing frequency of extreme El Niño events due to greenhouse warming. Nature Clim Change 4, 111–116 (2014). https://doi.org/10.1038/nclimate2100

505

506 Capet XJ, Marchesiello P., McWilliams JC (2004) Upwelling response to coastal wind profiles. Geophys Res Lett
507 31, L13311. doi:10.1029/2004GL020123

508

509 CERSAT (2002) Mean wind fields (MWF product) user manual volume 1: QuikSCAT. Rep C2-MUT-W-04-IF.
510 CERSAT-IFR- EMER, Brest

511

512 Chamorro A, Echevin V, Colas F, Oerder V, Tam J, Quispe-Ccalluari (2018) Mechanisms of the intensification of
513 the upwelling-favorable winds during El Niño 1997-1998 in the Peruvian Upwelling System, Clim Dyn (2018),
514 https://doi.org/10.1007/s00382-018-4106-6

515

516 Chavez FP, Bertrand A, Guevara-Carrasco R, Soler P, Csirke P (2008) The northern Humboldt Current System:
517 Brief history, present status and a view towards the future. Prog Oceanogr 79(2–4):95-105.
518 doi:10.1016/j.pocean.2008.10.012

519

520 Chen F, Dudhia J (2001) Coupling an advanced land surface hydrology model with the penn state-NCAR MM5
521 modeling system. Part ii: Preliminary model validation. Mon Weather Rev 129(4):587−604. doi:10.1175/1520-
522 0493(2001)129<0587:CAA LSH>2.0.CO;2

523

524 Chelton DB, Esbensen SK, Schlax MG, Thum N, Freilich MH, Wentz FJ, Gentemann CL, McPhaden MJ, Schopf
525 PS (2001) Observa- tions of coupling between surface wind stress and sea surface temperature in the Eastern Trop-
526 ical Pacific. J Clim 14:1479– 1498. doi:10.1175/1520-0442(2001)014<1479:OOCBSW>2.0 . CO;2

527

528 Cushing D (1990) Plankton production and year class strength in fish populations: an update of the match/mis-
529 match hypothesis. Advances in Marine Biology 26, 250–294.

530

Dudhia J (1989) Numerical study of convection observed during the winter monsoon experiment using a mesoscale two-dimensional model. J Atmos Sci 46:3077-3107. doi:10.1175/1520-0469(1989)046<3077:NSOCOD>2.0.CO;2.

Dutheil C, Bador M, Lengaigne M, Lefevre J, Jourdain N, Vialard J, Jullien S, Peltier A, Menkes C (2019) Impact of surface temperature biases on climate change projections of the South Pacific Convergence Zone. Clym Dym 53:3197-3219. doi:10.1007/s00382-019-04692-6.

Echevin, V., Aumont, O., Ledesma, J., Flores, G., 2008. The seasonal cycle of surface chlorophyll in the peruvian upwelling system: A modelling study. Progress In Oceanography 79, 167–176.

Echevin V, Colas F, Espinoza-Morriberon D, Vasquez L, Anculle T and Gutierrez D (2018) Forcings and Evolution of the 2017 Coastal El Niño Off Northern Peru and Ecuador. Front. Mar. Sci. 5:367. doi: 10.3389/fmars.2018.00367

Echevin, V., Gévaudan, M., Espinoza-Morriberón, D., Tam, J., Aumont, O., Gutierrez, D., and Colas, F. (2020) Physical and biogeochemical impacts of RCP8.5 scenario in the Peru upwelling system, Biogeosciences, 17, 3317–3341, https://doi.org/10.5194/bg-17-3317-2020.

Garreaud RD (2018) A plausible atmospheric trigger for the 2017 coastal El Niño. Int. J. Climatol. 38, e1296–e1302. doi: 10.1002/joc.5426

Goubanova, K., Echevin, V., Dewitte, B., Codron, F., Takahashi, K., Terray, P., Vrac, M., 2011. Statistical downscaling of sea-surface wind over the Peru-Chile upwelling region: Diagnosing the impact of climate change from the IPSL-CM4 model. Climate Dynamics 36 (7), 1365–1378.

Gutiérrez, D., Bouloubassi, I., Sifeddine, A., Purca, S., Goubanova, K., Graco, M., Field, D., Méjanelle, L., Velazco, F., Lorre, A., Salvatteci, R., Quispe, D., Vargas, G., Dewitte, B., and Ortlieb, L. (2011) Coastal cooling and

559 increased productivity in the main up- welling zone off Peru since the mid-twentieth century, Geophys. Res. Lett.,
560 38, L07603, https://doi.org/10.1029/2010GL046324.

561

562 Janjic ZI (1994) The step-mountain eta coordinate model: further developments of the convection, viscous sub-
563 layer, and turbulence closure schemes. Mon Wea Rev 122:927–945. doi:10.1175/1520-
564 0493(1994)122<0927:TSMECM>2.0.CO;2

565

566 Jebri, B., Khodri, M., Echevin, V., Gastineau, G., Thiria, S., Vialard, J., & Lebas, N. (2020). Contributions of in-
567 ternal variability and external forcing to the recent trends in the Southeastern Pacific and Peru-Chile upwelling sys-
568 tem. *Journal of Climate*, 2020. doi :10.1175/JCLI-D-19-0304.1

569

570 Kanamitsu M, Ebisuzaki W, Woollen J, Yang S-K, Hnilo JJ, Fiorino M, Potter GL (2002) NCEP–DOE AMIP-II
571 Reanalysis (R-2). Bulletin of the American Meteorological Society 83 (11), 1631–1644.

572

573 Kawase H, Yoshikane T, Hara M, Ailikun B, Kimura F, and Yasunari T (2008) Downscaling of the climatic
574 change in the mei-yu rainband in East Asia by a pseudo climate simulation method. SOLA, 4, 73-76,
575 doi:10.2151/sola.2008-019.

576

577 Kawase H, Yoshikane T, Hara M, Kimura F, Yasunari T, Ailikun B, Ueda H, and Inoue T (2009) Intermodel vari-
578 ability of future changes in the Baiu rainband estimated by the pseudo global warming downscaling method, J.
579 Geophys. Res., 114, D24110, doi:10.1029/2009JD011803.

580

581 Marti O, Braconnot P, Dufrense JL et al (2010) Key features of the IPSL ocean atmosphere model and its sensitiv-
582 ity to atmospheric resolution. Clim Dyn 34:1–26

583

584 Nakanishi M, Niino H (2009) Development of an improved turbulence closure model for the atmospheric bound-
585 ary layer. J Meteorol Soc Jpn 87:895–912. doi:10.2151/jmsj.87.895

586

Narayan N, Paul A, Mulitza S, Schulz M (2010) Trends in coastal upwelling intensity during the late 20th century. Ocean Science 6 (3), 815–823.

Mechoso, C. R., Wood, R., Weller, R., Bretherton, C. S., Clarke, A. D., Coe, H., Fairall, C., Farrar, T., Feingold, G., Garreaud, R., Grados, C., McWilliams, J., De Szoeke, S. P., Yuter, S. E., Zuidema, P., 2014. Ocean-cloud-atmosphere-land interactions in the southeastern pacific. Bulletin of the American Meteorological Society 95 (3), 357–375.

Mlawer E, Taubman S, Brown P, Iacono M, Clough S (1997) Radiative transfer for inhomogeneous atmosphere: RRTM, a validated correlated-k model for the long-wave. J Geophys Res 102:16,663–16,682. doi:10.1029/97JD00237

Oerder V, Colas F, Echevin V, Codron F, Tam J, Belmadani A (2015) Peru-Chile upwelling dynamics under climate change. J Geophys Res 120(2):1152-1172. doi: 10.1002/2014JC010299.

Oerder V, Colas F, Echevin V, Masson S, Hourdin C, Jullien S, Gurvan M, Lemarié F (2016) Mesoscale SST-wind stress coupling in the Peru–Chile current system: which mechanisms drive its seasonal variability? Clim Dyn 47:2309. doi:10.1007/s00382-015-2965-7

Oerder V, Colas F, Echevin V, Masson S, and Lemarié F (2018) Impacts of the mesoscale ocean-atmosphere coupling on the Peru-Chile ocean dynamics: the current-induced wind stress modulation. J. Geophys. Res. Oceans 123, 812–833. doi: 10.1002/2017JC013294

Oyarzún D and Brierley CM (2019) The future of coastal upwelling in the Humboldt current from model projections, Clim. Dynam., 52, 599–615

613 Perlin N, Skyllingstad E, Samelson R (2011) Coastal Atmospheric Circulation around an Idealized Cape during
614 Wind-Driven Upwelling Studied from a Coupled Ocean-Atmosphere Model. Monthly Weather Review 139, 809–
615 829.

616

617 Reynolds RW, Smith TM, Liu C, Chelton DB, Casey KS, Schlax MG (2007) Daily high-resolution-blended analy-
618 ses for sea surface temperature. J Climate 20:5473-5496. doi:10.1175/2007JCLI1824.1.

619

620 Rykaczewski, R. R., J. P. Dunne, W. J. Sydeman, M. García-Reyes, B. A. Black, and S. J. Bograd (2015), Pole-
621 ward displacement of coastal upwelling-favorable winds in the ocean's eastern boundary currents through the 21st
622 century, Geophys. Res. Lett., 42, 6424–6431.

623

624 Skamarock W, Klemp J (2008) A time-split nonhydrostatic atmos- pheric model for weather research and forecast-
625 ing applications. J Comp Phys 227:3465–3485. doi:10.1016/j.jcp.2007.01.037

626

627 Small R J, and Coauthors (2008) Air–sea interaction over ocean fronts and eddies. Dyn. Atmos. Oceans, 45, 274–
628 319, doi:10.1016/j.dynatmoce.2008.01.001.

629

630 Soares PMM, Lima DCA, Semedo A, Cardoso RM, Cabos W, Sein D (2018) The North African coastal low level
631 wind jet: a high resolution view. Climate Dynamics, 1–20.

632

633 Sydeman W J, García-Reyes M, Schoeman D S, Rykaczewski R R, Thompson S A, Black B A, Bograd S J (2014)
634 Climate change and wind intensification in coastal upwelling ecosystems. Science 345 (6192), 77–80.

635

636 Takahashi K, and Martínez AG (2017) The very strong coastal El Niño in 1925 in the far-eastern Pacific. Clim.
637 Dyn. 1–27. doi: 10.1007/s00382-017-3702-1

638

van Vuuren DP, Edmonds J, Kainuma M, Riahi K, Thomson A, Hibbard K, Hurtt GC, Kram T, Krey V, Lamarque JF, Masui T, Meinshausen M, Nakicenovic N, Smith SJ, Rose SK (2011) The representative concentration pathways: An overview. Climatic Change 109 (1), 5–31.

Wang, D., Gouhier, T. C., Menge, B. A., & Ganguly, A. R. (2015). Intensification and spatial homogenization of coastal upwelling under climate change. Nature, 518(7539), 390-394.

Yeh S, Kug J, Dewitte B, Kwon M-H, Kirtman B.P., Jin F-F (2009) El Niño in a changing climate. Nature 461, 511–514. https://doi.org/10.1038/nature08316

7. Tables

Tabla 1. Name and characteristics of the CMIP5 models. The numbers are used in Figures 3 and 13.

8. Figure captions.

Figure 1. Projected changes in a) mean wind speed (in m s^{-1}, colors) and wind direction (arrows), and b) annual cycle of upwelling-favorable alongshore wind (color shading in m s^{-1}, contours for relative change (in %)) off Peru-Chile, for the 2080-2100 period relative to the 1989-2009 period by the multi-model mean of 31 CMIP5 global models under the RCP8.5 scenario. Regions where more than 75% models agree on the sign of wind speed change are indicated with red dots in Figure 1a. The alongshore wind is averaged in a 100-km coastal band in Figure 1b.

Figure 2. a) The three model domains used in the WRF simulations: d01, d02 and d03, with horizontal resolution of 105, 21 and 7 km, respectively. b) Model topography (in meters) above sea level for the innermost domain with 7 km of resolution.

Figure 3. Projected changes for the 2080-2100 period relative to the 1989-2009 under the RCP8.5 scenario for a) the mean sea surface temperature (in °C) from the multi-model mean of 31 CMIP5 models, and for b) the alongshore SST gradient (in 10^{-3}°C km^{-1}) off Peru (5-9°S minus 9-13°S averaged within a 200-km coastal band indi-

667 cated in Fig. 3a by red boxes) from individual climate models (see Table 1) and from the multi-model mean (with
668 blue whisker indicating the intermodel standard deviation). Red bars correspond to the CMIP5 models used to run
669 sensitivity experiments.

670

671 Figure 4. Mean surface wind (in m s^{-1}) for the period 2000-2003 from a) WRF105, b) WRF21, c) WRF7 simula-
672 tions, and d) QuikSCAT satellite observations. e) Mean wind speed cross-shore profile averaged alongshore be-
673 tween 7°S and 13°S. The vertical dotted line in e) indicates the offshore distance of the satellite blind zone.

674

675 Figure 5. Mean annual cycle of alongshore wind (averaged in a coastal band of ~100 km) from a) WRF7 and b)
676 QuikSCAT satellite over the period 2000-2003. c) Map of the differences between model and observations
677 (WRF7-QuikSCAT). High resolution model data was interpolated on the 1/4° QuikSCAT grid. Units are in m s^{-1}.

678

679 Figure 6. Mean surface wind (in m s^{-1}) under the RCP8.5 scenario (2086-2095 period) from a) WRF21 and d)
680 WRF7. Projected change (2086-2095 minus 1994-2003) in mean surface wind from b) WRF21 and e) WRF7. Pro-
681 jected relative change (color shading in m s^{-1} and contours in %) in the mean seasonal cycle of alongshore winds
682 (in a coastal band of ~100 km) from c) WRF21 and f) WRF7.

683

684 Figure 7. WRF105 mean sea level pressure (in hPa) for the retrospective period (1994-2003, white contours), un-
685 der the RCP8.5 scenario (2086-2095, black contours), and sea level pressure change (2086-2095 minus 1994-2003,
686 color shading) for a) summer (JFM) and b) winter (JAS).

687

688 Figure 8. a) Projected surface wind change (in m s^{-1}, 2086-2095 minus 1994-2003) under RCP8.5 scenario and b)
689 monthly alongshore momentum budget for the historical period (1994-2003) over coastal boxes indicated in Fig
690 8a, in summer (January-March). c) Projected change (in m s^{-1}, 2086-2095 minus 1994-2003) in the monthly
691 alongshore momentum budget under RCP8.5 summer conditions. ADV, PGF, COR and MIX are acronyms used
692 for advection, pressure gradient, Coriolis and vertical turbulent mixing forces contribution, respectively.

693

694 Figure 9. Same as Fig. 8 but for winter (July-September)

Figure 10. a) Total advection of meridional momentum in May-August for the retrospective period (1994-2003) and b) the meridional advection term (-V.∂V/∂y). Arrows in a) indicate the averaged surface winds (in m s^{-1}). Projected change in c) total advection of meridional momentum and in d) meridional advection term in May-August under RCP8.5 conditions. Units are in 10^{-4} m s^{-2}.

Figure 11. Projected change (in m s^{-1}, 2086-2095 minus 1994-2003, color shading) in the mean seasonal cycle of alongshore winds (in a coastal band of ~100 km) under RCP8.5 conditions from WRF21 sensitivity experiments forced by SST from a) CNRM-CM5, b) CESM1-CAM5 and c) CSIRO-Mk3-6-0 (see red bars in Fig.3b). Black contours indicate the absolute wind change as a percentage (%) of the value of the alongshore wind over the retrospective period (1994-2003).

Figure 12. Scatter plots of monthly mean coastal wind (in %) and alongshore SST gradient change (in 10^{-3}°C km^{-1}) from the three sensitivity experiments (WRF-cnrm, WRF-csiro and WRF-cesm1 with square, circles and diamond marks, respectively) and from the ensemble-mean climate change simulation (stars). Alongshore wind in the a) North (4-9°S), b) Central (9-14°S) and c) South (14-18°S) of Peru are shown. Data and linear fits for each seasons (Fall-Winter and Spring-Summer) are shown in blue and red colors respectively. Linear fits for the annual mean values are shown in black. The change in alongshore SST gradient is computed for the north, central and south coasts as the mean coastal SST difference between 4°S-9°S minus 9°S-14°S, 9°S-14°S minus 14°S-19°S, and 14°S-18°S minus 18°S-22°S, respectively. Note the change of horizontal and vertical scales in the different panels.

Figure 13. a) Sea level pressure (in hPa) for the 2080-2100 period (black contours), for the historical 1989-2009 period (white contours), and sea level pressure change (2080-2100 minus 1989-2009, in hPa, color shading). SLP is computed from the multi model mean of 31 CMIP5 models under the RCP8.5 scenario. Scatter plots of b) mean coastal wind change along 7-11°S (in %) versus the large-scale meridional sea level pressure gradient change (in 10^{-4} hPa km^{-1}), and c) mean coastal wind change versus the alongshore SST gradient change (in 10^{-3} °C km^{-1}) off Peru coast. Each number (from 1 to 31) indicates a particular CMIP5 model value under the RCP8.5 scenario (see Table 1 and Figure 3). Black, red and blue numbers correspond to annual, summer-spring and fall-winter

724 mean values, respectively. Linear regression lines for annual, summer-spring and fall-winter mean values are
725 shown in black, red and blue, respectively.

Figure 1.

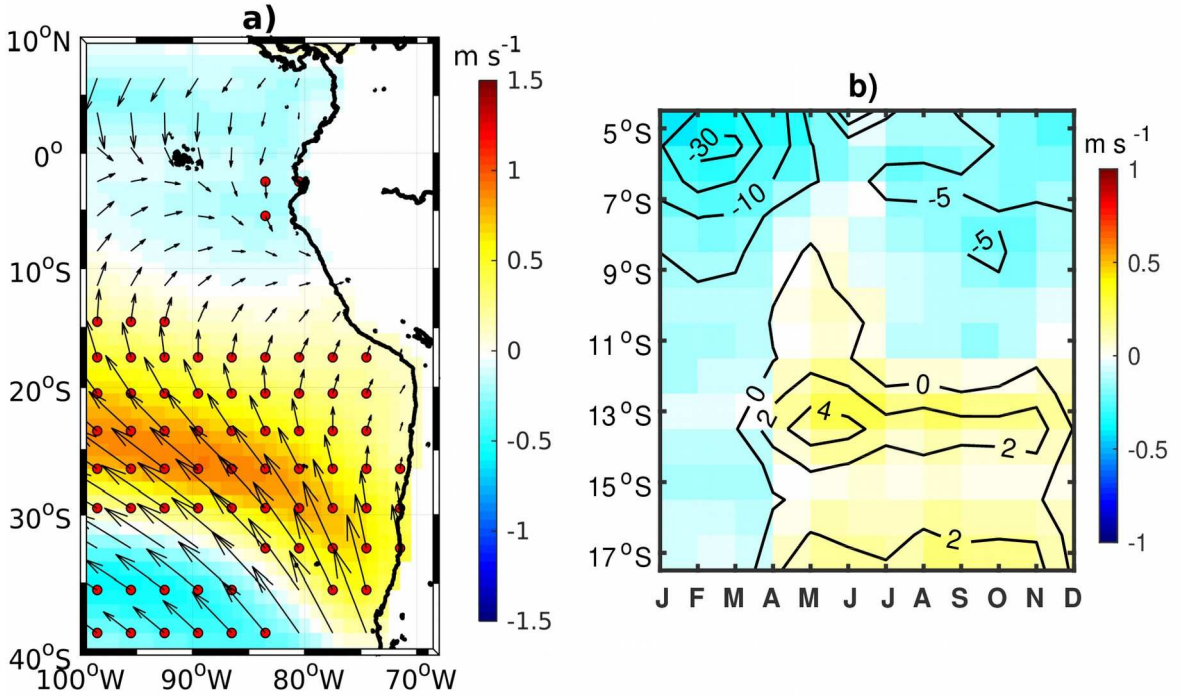
a)
10°N
0°
10°S
20°S
30°S
40°S
100°W
90°W
80°W
70°W
m s-1
1.5
1
0.5
0
-0.5
-1
-1.5
b)
5°S
7°S
9°S
11°S
13°S
15°S
17°S
J F M A M J J A S O N D
-30
-10
-5
-5
0
2
4
2
2
m s-1
1
0.5
0
-0.5
-1

Figure 2.

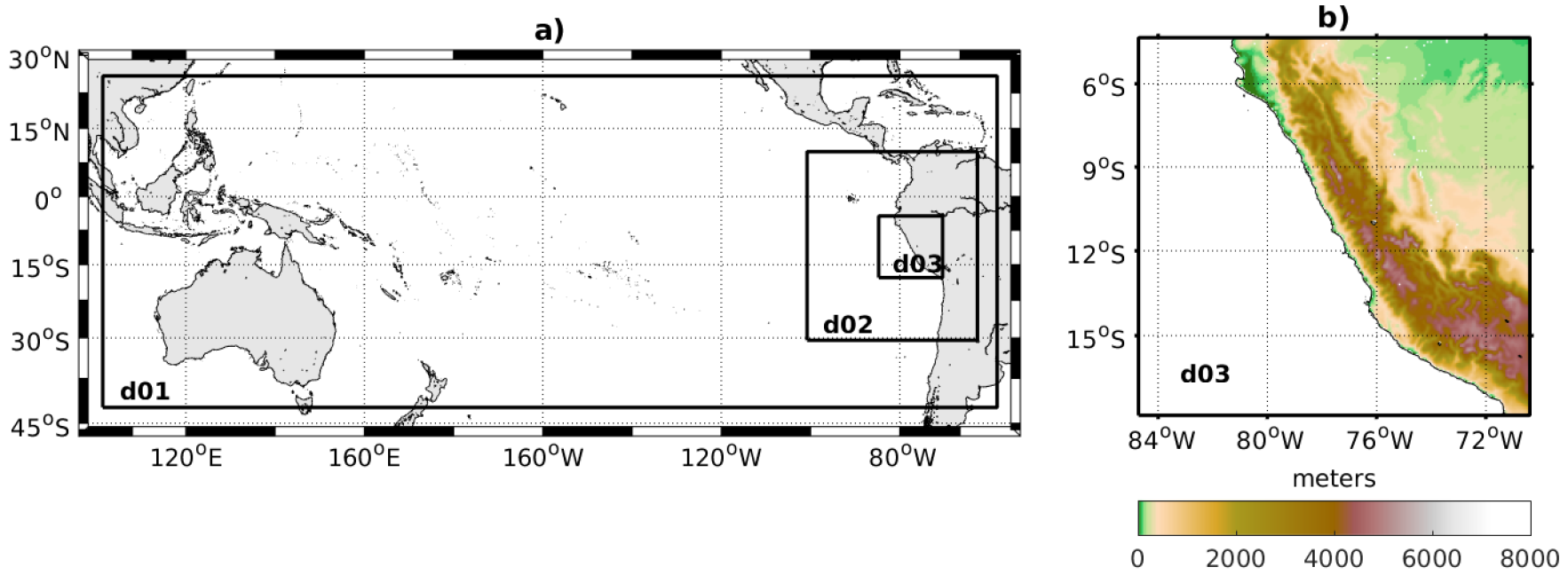
a)
30°N
15°N
0°
15°S
30°S
45°S
120°E
160°E
160°W
120°W
80°W
d01
d02
d03
b)
6°S
9°S
12°S
15°S
84°W
80°W
76°W
72°W
d03
meters
0
2000
4000
6000
8000

Figure 3.

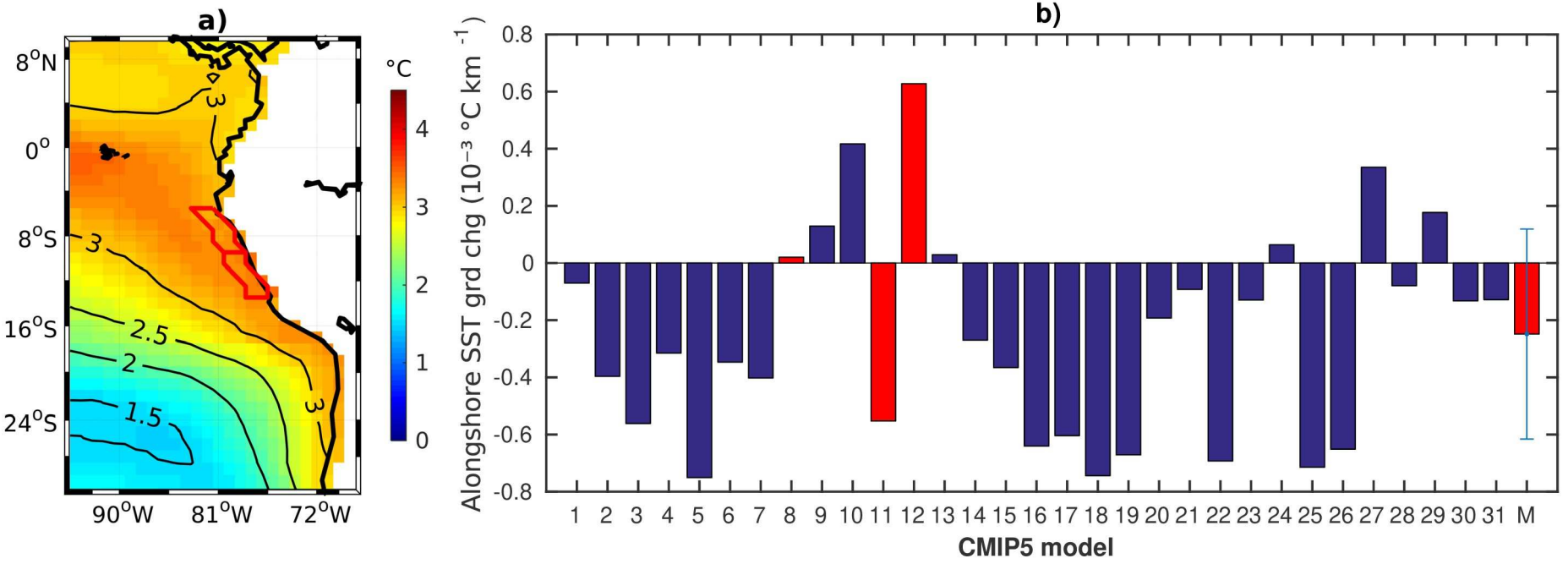
a)
8°N
0°
8°S
16°S
24°S
90°W
81°W
72°W
°C
4
3
2
1
0
3
2.5
2
1.5
b)
Alongshore SST grd chg (10⁻³ °C km⁻¹)
0.8
0.6
0.4
0.2
0
-0.2
-0.4
-0.6
-0.8
1 2 3 4 5 6 7 8 9 10 11 12 13 14 15 16 17 18 19 20 21 22 23 24 25 26 27 28 29 30 31 M
CMIP5 model

Figure 4.

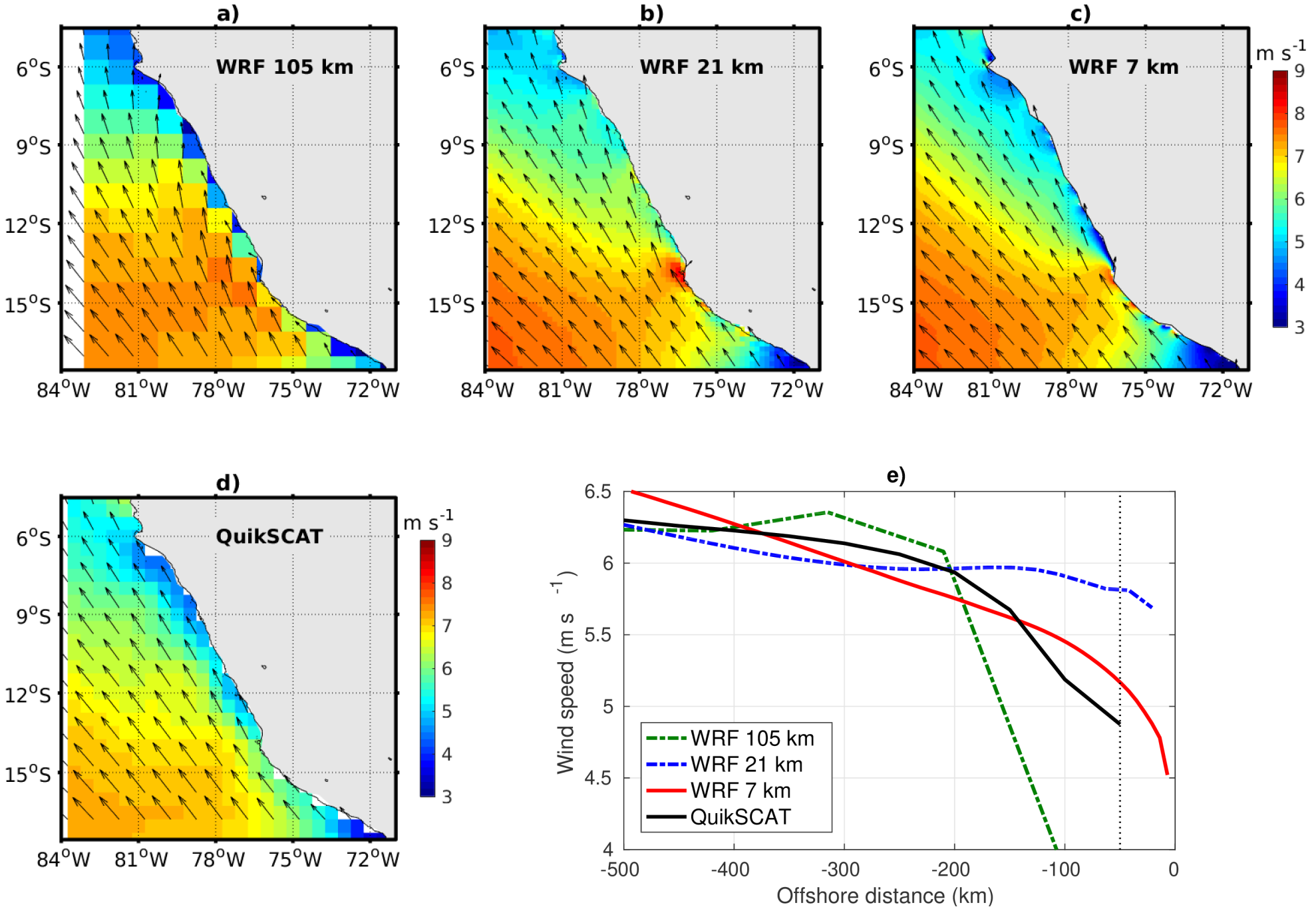
a)
WRF 105 km
b)
WRF 21 km
c)
WRF 7 km
m s-1
9
8
7
6
5
4
3
6°S
9°S
12°S
15°S
84°W
81°W
78°W
75°W
72°W
d)
QuikSCAT
e)
Wind speed (m s-1)
Offshore distance (km)
6.5
6
5.5
5
4.5
4
-500
-400
-300
-200
-100
0
WRF 105 km
WRF 21 km
WRF 7 km
QuikSCAT

Figure 5.

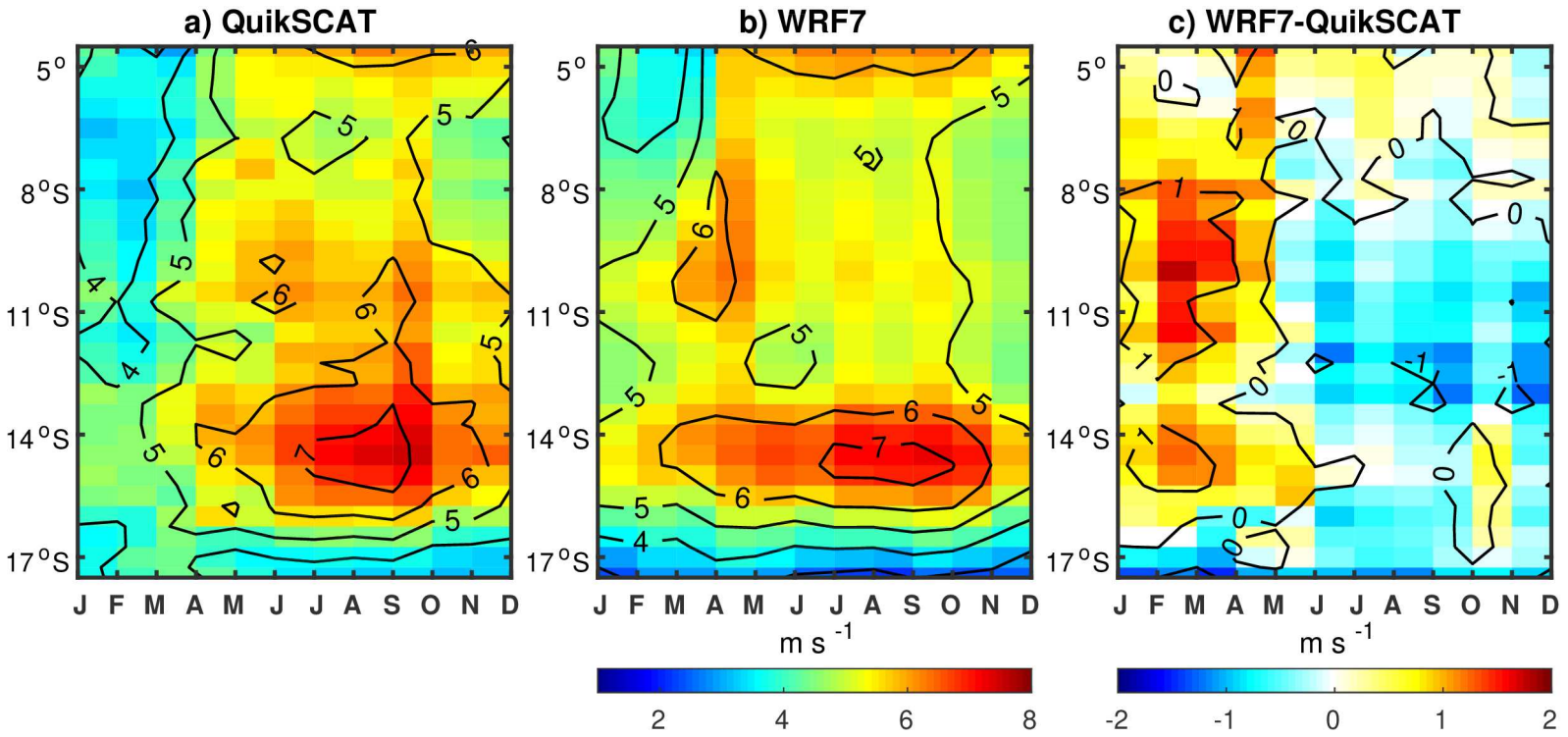
a) QuikSCAT
b) WRF7
c) WRF7-QuikSCAT
5°
8°S
11°S
14°S
17°S
J F M A M J J A S O N D
m s -1
2 4 6 8
-2 -1 0 1 2

Figure 6.

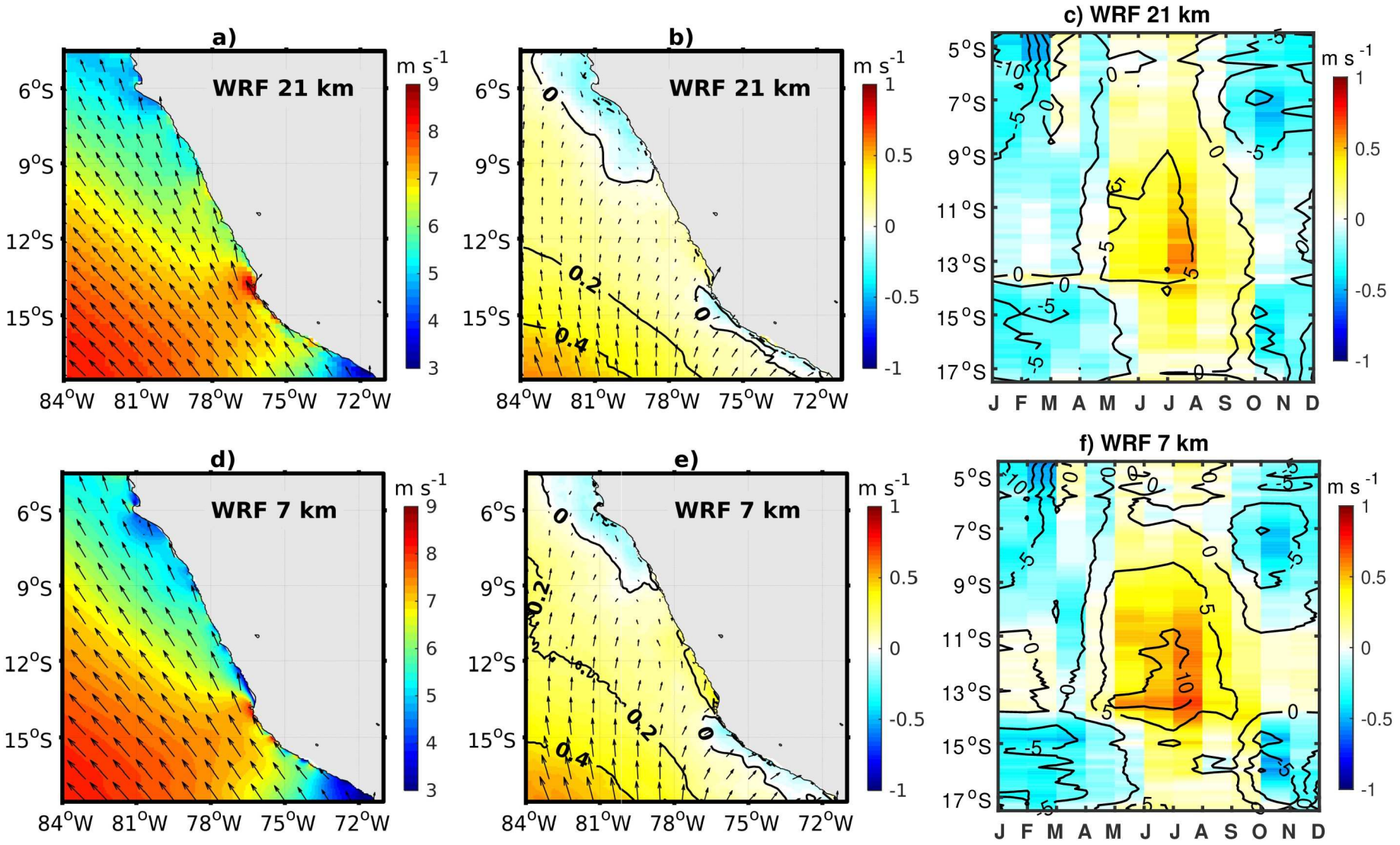
a)
WRF 21 km
m s-1
b)
WRF 21 km
m s-1
c) WRF 21 km
m s-1
d)
WRF 7 km
m s-1
e)
WRF 7 km
m s-1
f) WRF 7 km
m s-1
6°S
9°S
12°S
15°S
5°S
7°S
11°S
13°S
17°S
84°W 81°W 78°W 75°W 72°W
J F M A M J J A S O N D

Figure 7.

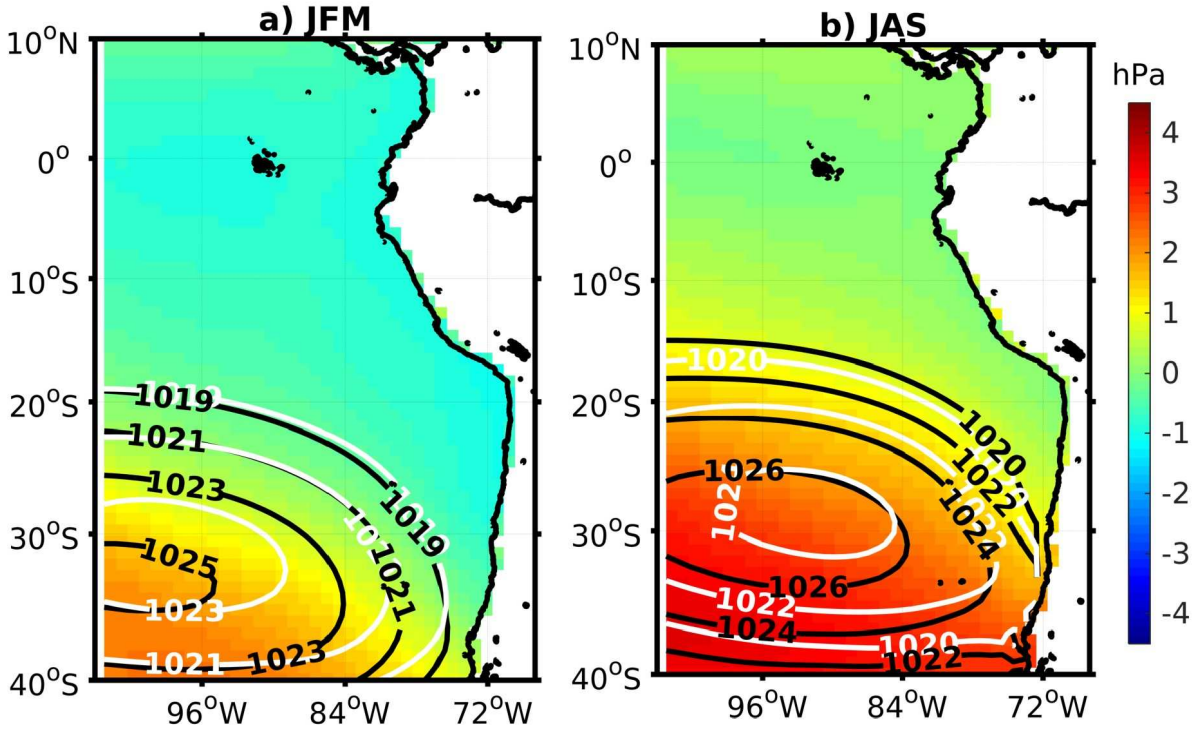
a) JFM
b) JAS
10°N
0°
10°S
20°S
30°S
40°S
96°W
84°W
72°W
1019
1021
1023
1025
1020
1022
1024
1026
hPa
4
3
2
1
0
-1
-2
-3
-4

Figure 8.

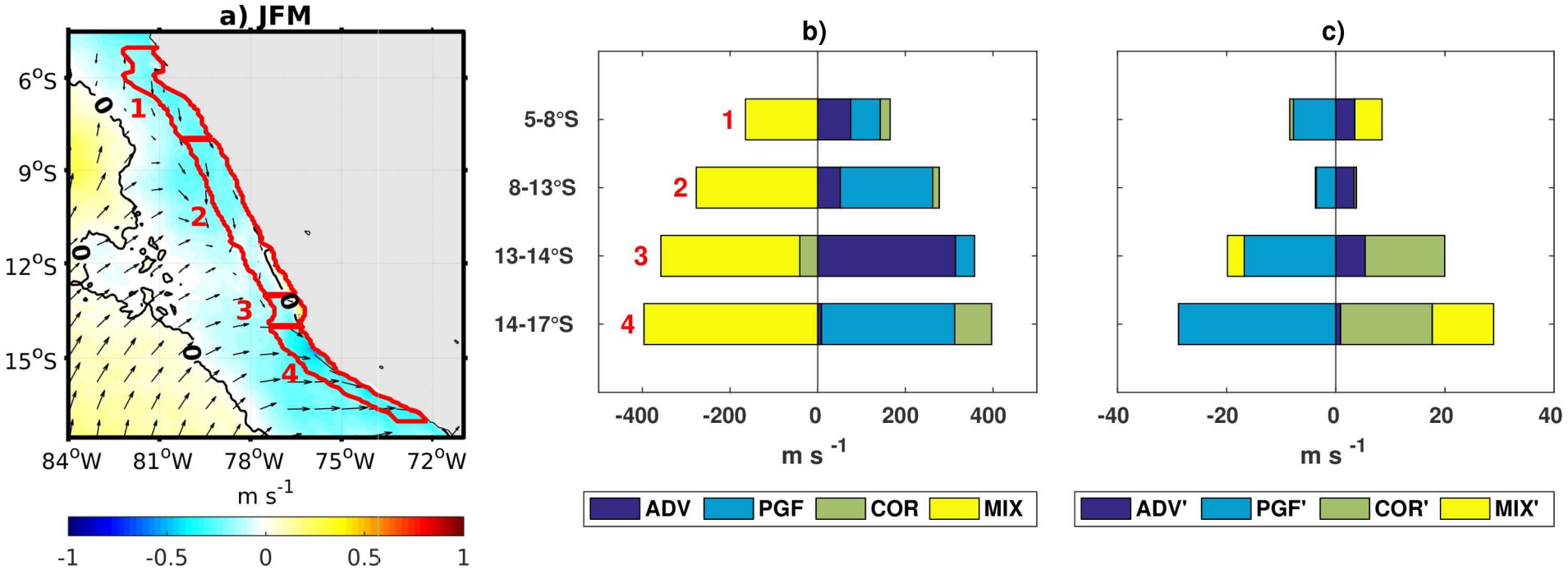
a) JFM
6°S
9°S
12°S
15°S
84°W
81°W
78°W
75°W
72°W
m s-1
-1
-0.5
0
0.5
1
1
2
3
4
0
b)
5-8°S
8-13°S
13-14°S
14-17°S
-400
-200
0
200
400
m s -1
ADV
PGF
COR
MIX
c)
-40
-20
0
20
40
m s -1
ADV'
PGF'
COR'
MIX'

Figure 9.

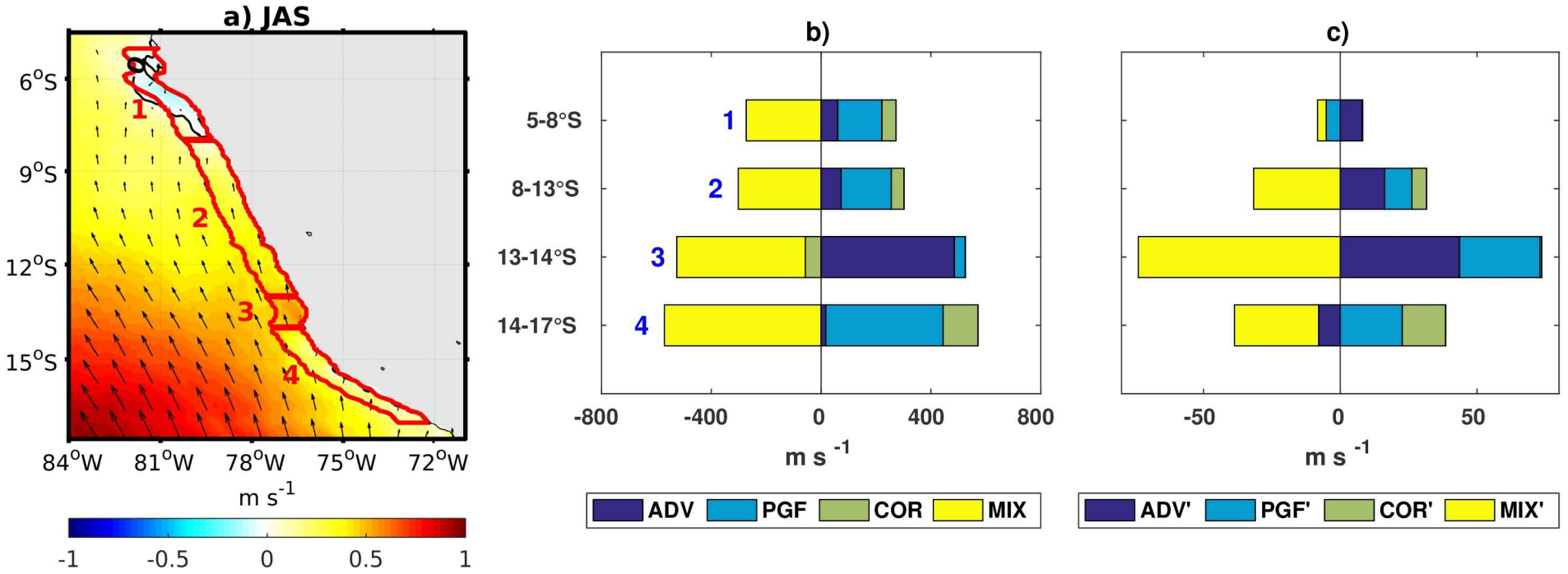
a) JAS
6°S
9°S
12°S
15°S
84°W
81°W
78°W
75°W
72°W
m s-1
-1
-0.5
0
0.5
1
1
2
3
4
b)
5-8°S
8-13°S
13-14°S
14-17°S
-800
-400
0
400
800
m s -1
ADV
PGF
COR
MIX
c)
-50
0
50
m s -1
ADV'
PGF'
COR'
MIX'

Figure 10.

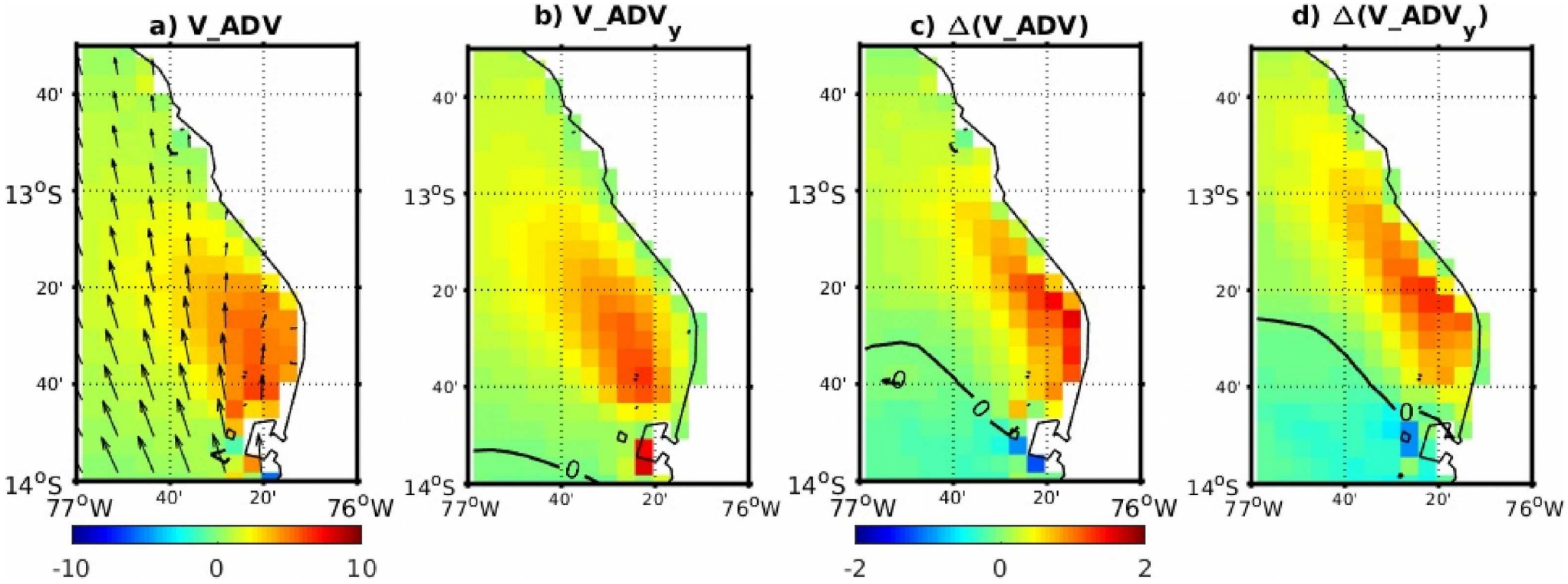

Figure 11.

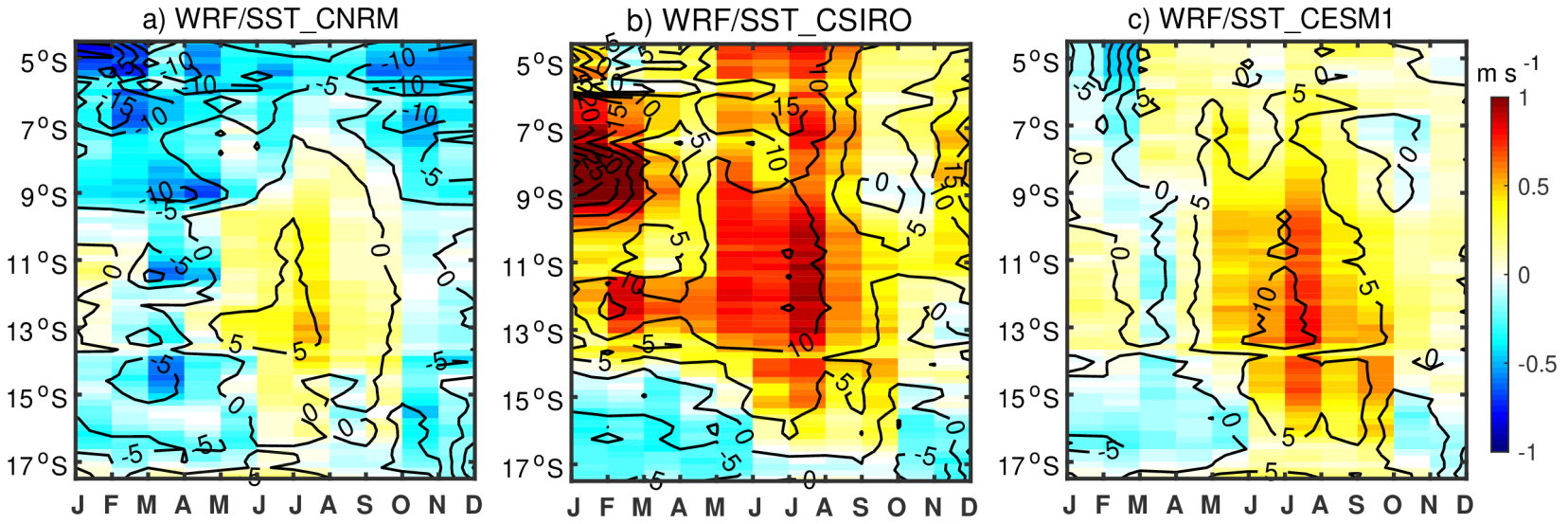
a) WRF/SST_CNRM
b) WRF/SST_CSIRO
c) WRF/SST_CESM1
5°S
7°S
9°S
11°S
13°S
15°S
17°S
J F M A M J J A S O N D
m s -1
1
0.5
0
-0.5
-1

Figure 12.

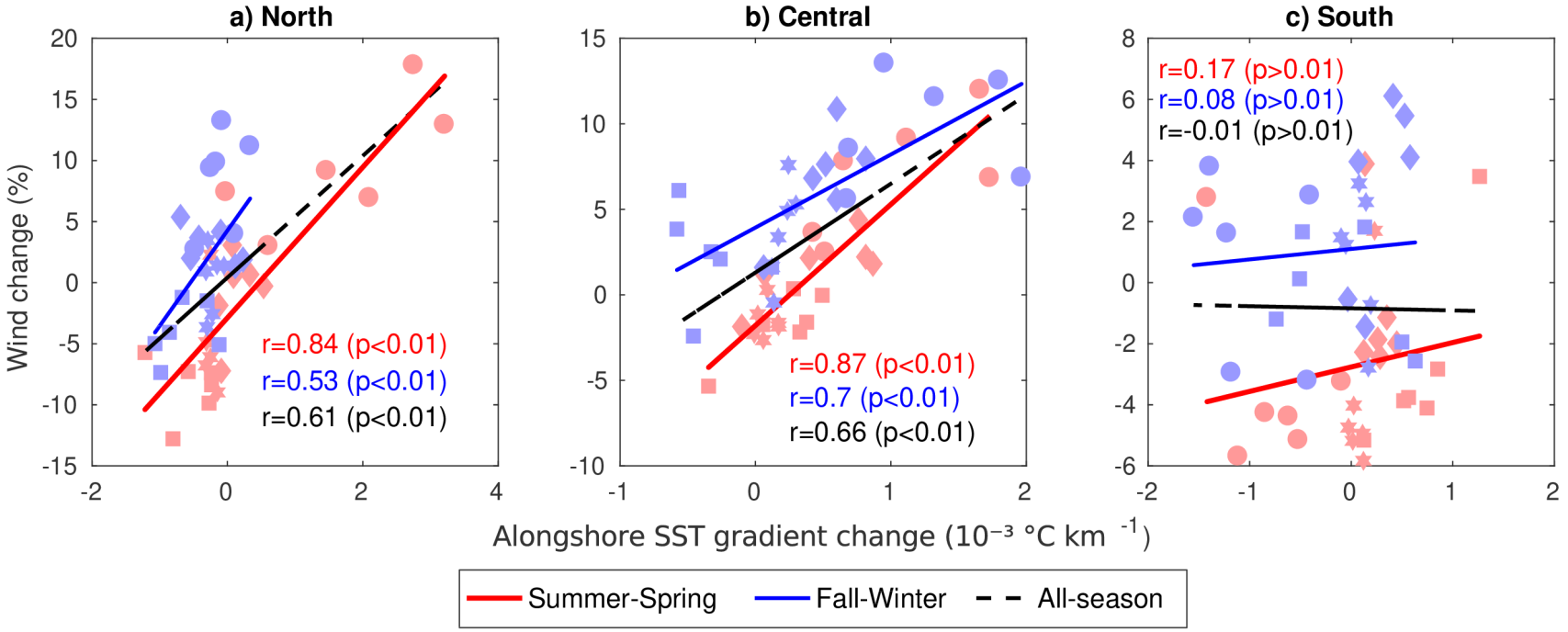
a) North
b) Central
c) South
Wind change (%)
Alongshore SST gradient change (10⁻³ °C km ⁻¹)
r=0.84 (p<0.01)
r=0.53 (p<0.01)
r=0.61 (p<0.01)
r=0.87 (p<0.01)
r=0.7 (p<0.01)
r=0.66 (p<0.01)
r=0.17 (p>0.01)
r=0.08 (p>0.01)
r=-0.01 (p>0.01)
Summer-Spring
Fall-Winter
All-season

Figure 13.

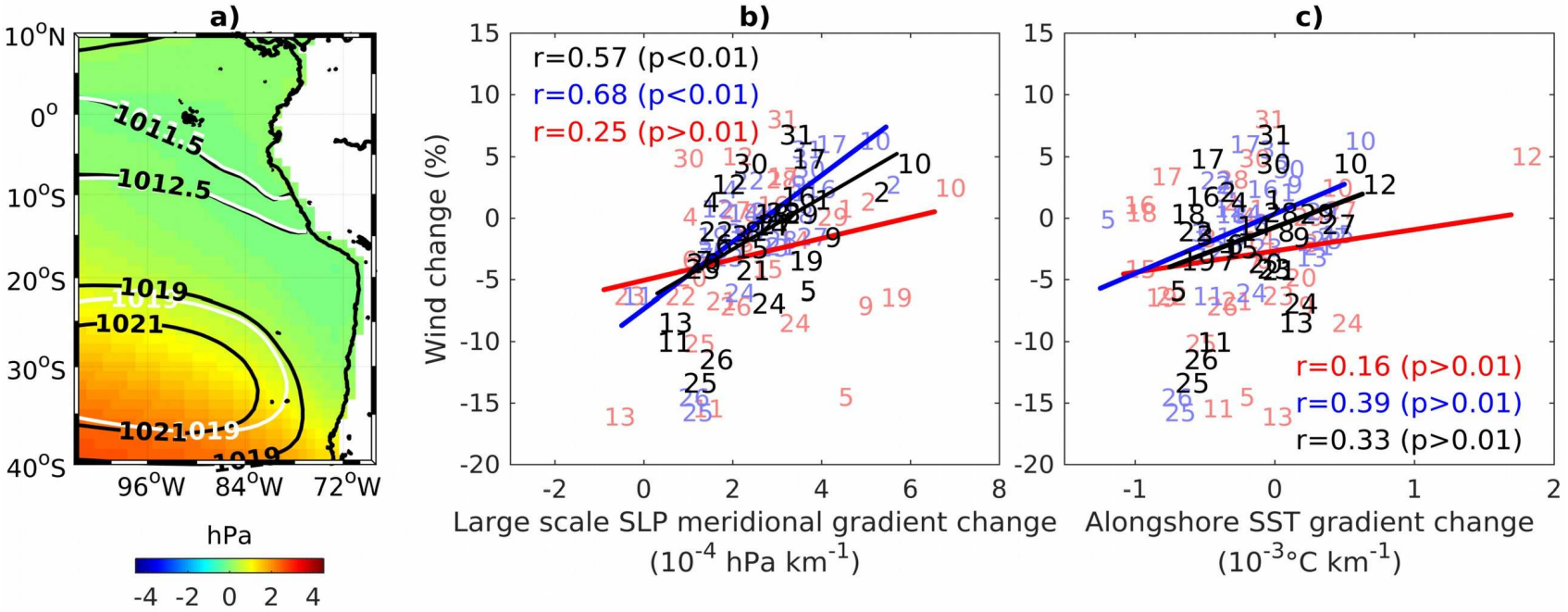
a)
10°N
0°
10°S
20°S
30°S
40°S
96°W
84°W
72°W
1011.5
1012.5
1019
1021
hPa
-4 -2 0 2 4
b)
r=0.57 (p<0.01)
r=0.68 (p<0.01)
r=0.25 (p>0.01)
Wind change (%)
Large scale SLP meridional gradient change
(10-4 hPa km-1)
c)
r=0.16 (p>0.01)
r=0.39 (p>0.01)
r=0.33 (p>0.01)
Alongshore SST gradient change
(10-3°C km-1)